Paleoearthquakes of the past 30,000 years along the North Tehran Fault (Iran)

J.F. Ritz, Amid Nazari, S. Balescu, M. Lamothe, Reza Salamati, A. Ghassemi, A. Shafei, M. Ghorashi, A. Saidi

Paleoearthquakes of the past 30,000 years along the North Tehran Fault (Iran)

J.-F. Ritz,[1] H. Nazari,[1,2] S. Balescu,[3] M. Lamothe,[4] R. Salamati,[5] A. Ghassemi,[5] A. Shafei,[5] M. Ghorashi,[2] and A. Saidi[2]

Received 10 January 2012; revised 20 April 2012; accepted 20 April 2012; published 7 June 2012.

[1] The North Tehran Fault (NTF) is located at the southernmost piedmont of Central Alborz and crosses the northern suburbs of the Tehran metropolis and adjacent cities, where ~15 million people live. Extending over a length of about 110 km, the NTF stands out as a major active fault and represents an important seismic hazard for the Iranian capital after historical seismicity. In order to characterize the activity of the NTF in terms of kinematics, magnitude and recurrence intervals of earthquakes, we carried out a first paleoseismological study of the fault within its central part between Tehran and Karaj cities. We opened a trench across a 3 m-high fault scarp affecting Quaternary deposits. Our study shows that the scarp is the result of repeated events along a main N115°E trending shallow dipping thrust fault, associated with secondary ruptures. From the trench analysis and Infrared Stimulated Luminescence (IRSL) dating of fault-related sediments, we interpreted between 6 and 7 surface-rupturing events that occurred during the past 30 kyrs. Their magnitudes (estimated from the displacements along the faults) are comprised between 6.1 and 7.2. The two last events – the largest - occurred during the past 7.9 ± 1.2 ka, which yields a Holocene slip rate of ~0.3 mm/yr. The 7 earthquakes scenario suggests a regular periodicity with a mean recurrence interval of ~3.8 kyrs. However, the two most recent events could correspond to the two largest historical earthquakes recorded in the area (in 312–280 B.C. and 1177 A.D.), and therefore suggest that the NTF activity is not regular.

Citation: Ritz, J.-F., H. Nazari, S. Balescu, M. Lamothe, R. Salamati, A. Ghassemi, A. Shafei, M. Ghorashi, and A. Saidi (2012), Paleoearthquakes of the past 30,000 years along the North Tehran Fault (Iran), *J. Geophys. Res.*, *117*, B06305, doi:10.1029/2012JB009147.

1. Introduction

[2] The North Tehran Fault (NTF) is located at the southernmost piedmont of Central Alborz Mountain range and crosses the northern suburbs of the Tehran metropolis (Figures 1 and 2a), which is one of the largest urban populated areas in the world (population for Tehran and its surroundings cities is ~15 millions). The NTF is described as an active thrust fault [e.g., *Tchalenko*, 1975] and could be the source of large-magnitude earthquakes in 312–280 B.C., 855 A.D. and 1177 A.D. [*Ambraseys and Melville*, 1982; *Berberian and Yeats*, 1999]. According to the historical records, the three events have destroyed the city of Ray which corresponds nowadays to the southern suburbs of Tehran (Figure 1).

[3] However, despite the historical data, the recent activity (i.e., Holocene-Upper Pleistocene ruptures) of the North Teheran Fault remains poorly documented [e.g., *Tchalenko et al.*, 1974]. No paleoseismological study has been carried out so far, and the lack of geological data attesting of the Holocene activity of the fault is due to the difficulty to follow the trace of the fault at the surface. The rapid and extensive urban development of the city of Tehran, especially during the last 20 years, has erased or buried most of the escarpments that could be still observed 50 years ago, at the time where Tehran was not yet a sprawling metropolis.

[4] Using 1/50,000 scale aerial pictures taken in 1955, we have been able to recognize a preserved fault scarp along the NTF trace and to target a first paleoseismological study of the North Tehran fault within its central part (location in Figure 2) between the megacity of Tehran and the city of Karaj. This study although preliminary (only one trench along a short fault section) represents the first paleoseismic

[1]Géosciences Montpellier, UMR 5243 (CNRS), Université Montpellier 2, Montpellier, France.
[2]Research Institute for Earth Sciences, Geological Survey of Iran, Tehran, Iran.
[3]Laboratoire Halma Ipel, UMR 8164 (CNRS), Université Lille 1, Villeneuve d'Ascq, France.
[4]Laboratoire de Luminescence LUX, Département des Sciences de la Terre et de l'Atmosphère, Université du Québec à Montréal, Montréal, Canada.
[5]Geological Survey of Iran, Tehran, Iran.

Corresponding author: J.-F. Ritz, Géosciences Montpellier, UMR 5243 (CNRS), Université Montpellier 2, F-34095 Montpellier CEDEX 05, France. (ritz@gm.univ-montp2.fr)

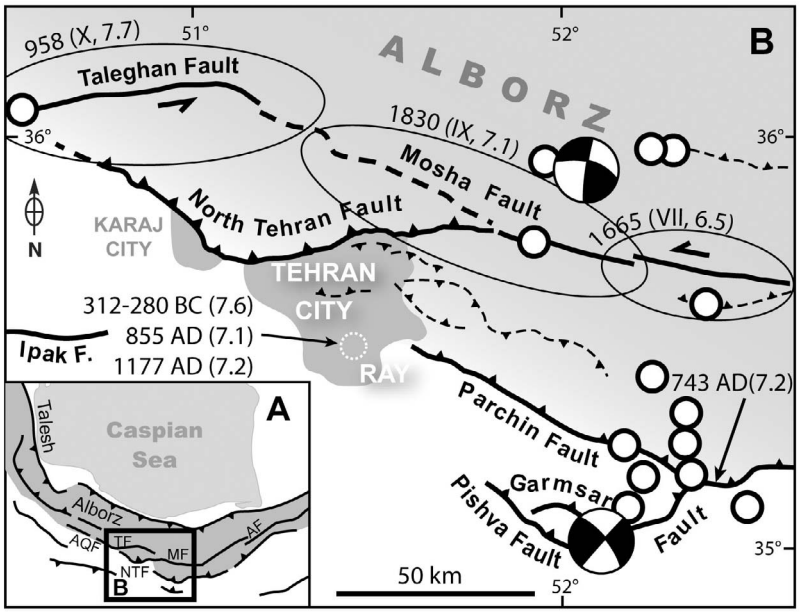

Figure 1. (a) Sketch map of the Alborz mountain range surrounding the South-Caspian basin and its main active faults. NTF: North Tehran Fault, TF: Taleghan Fault, MF: Mosha Fault, AQF: Abyek-Qazvin Fault, AF: Astaneh Fault. (b) Simplified map of the main faults considered as active in Tehran region (modified after *Nazari et al.*, 2010) with associated historical seismicity showing epicentral areas with the date, MSK intensity and estimated magnitude after the distribution and amount of damages (after *Ambraseys and Melville* [1982] and *Berberian and Yeats* [1999]). Grey: Alborz reliefs; White: alluvial piedmont; black lines with triangles: thrust faults; black lines with arrows: strike-slip faults; dashed lines: uncertain active faults. The shaded areas at the foothills of the Alborz Mountains represent Tehran and Karaj cities. Note that the sources of the 312–280 B.C., 855 A.D. and 1177 A.D. historical events that destroyed the old city of Ray (corresponding nowadays to the southern suburbs of Tehran; dotted circle) are not known or uncertain (*Berberian and Yeats* [2001] placed the 312–280 B.C. event at the junction between the Parchin and the Garmsar faults, at the same location than the 743 A.D. earthquake). The instrumental seismicity (Mb > 4.5 [*Engdahl et al.*, 1998]) is shown by white circles. Body wave modeled mechanisms [*Jackson et al.*, 2002] are shown by black focal spheres.

investigation along the NTF zone. It contributes to fill the gap of knowledge concerning its recent activity, providing the first quantitative data for the assessment of the seismic hazard in terms of kinematics, magnitude and recurrence intervals of earthquakes.

2. Tectonic Setting

[5] The North Tehran Fault corresponds to a crustal-scale structure, bounding the Central Alborz mountain range [e.g., *Allen et al.*, 2003; *Guest et al.*, 2006]. Inherited from a localized rifting process in Paleocene, the NTF has been reversed during Neogene times [*Nazari*, 2006]. At present, the NTF is involved in a regional transpressional strain process affecting the entire Alborz mountain range, which is partitioned between reverse faulting and left-lateral shearing [*Jackson et al.*, 2002; *Allen et al.*, 2003; *Ritz et al.*, 2006; *Hollingsworth et al.*, 2008, 2010; *Ritz*, 2009]. The NTF would absorb part of the 5 ± 2 mm/yr of NS shortening recorded across the Central Alborz by GPS [*Vernant et al.*, 2004], while most of the 4 ± 2 mm/yr of left-lateral shearing measured also by GPS across the range would be absorbed along the Mosha fault and the Taleghan fault [*Ritz et al.*, 2006; *Nazari et al.*, 2009a; *Landgraf et al.*, 2009; *Solaymani et al.*, 2011] (Figure 1).

[6] The NTF extends over approximately 110 km, between the western extremity of the Taleghan fault and the Mosha fault to the East (Figure 1). Also named the Farahzad-Karaj Thrust [*Guest et al.*, 2006], it is classically described as a thrust fault juxtaposing volcano-sedimentary Palaeocene series on Plio-Quaternary detrital sediments [e.g., *Berberian et al.*, 1985; *Ballato et al.*, 2008]. The fault shows a general "V" shape switching from the NW-SE direction to NE-SW between the cities of Karaj and Tehran (Figures 1 and 2a). Along its NE-SW trending branch, recent morphotectonics studies show that previous Cainozoic overthrusting features are sealed by overlapping deposits attesting of the inactivity of the ancient NTF [e.g., *Abbassi and Farbod*, 2009]. The fault activity appears now distributed on several newly formed fault segments showing a strong left-lateral strike-slip component, [*Landgraf et al.*, 2009; *Solaymani et al.*, 2011] (Figure 3). The active NE-SW trending branch of the NTF can be subdivided in three right-stepping fault segments: from the junction with the Mosha fault, a 25 km long slightly curved fault section defined a first segment, starting with an E-W direction and curving progressively to a ENE-WSW direction. A second segment (called the Niavaran F.) also trending ENE-WSW continues westward over a distance of 15 km. Clear evidences of left-lateral strike-slip displacements have been

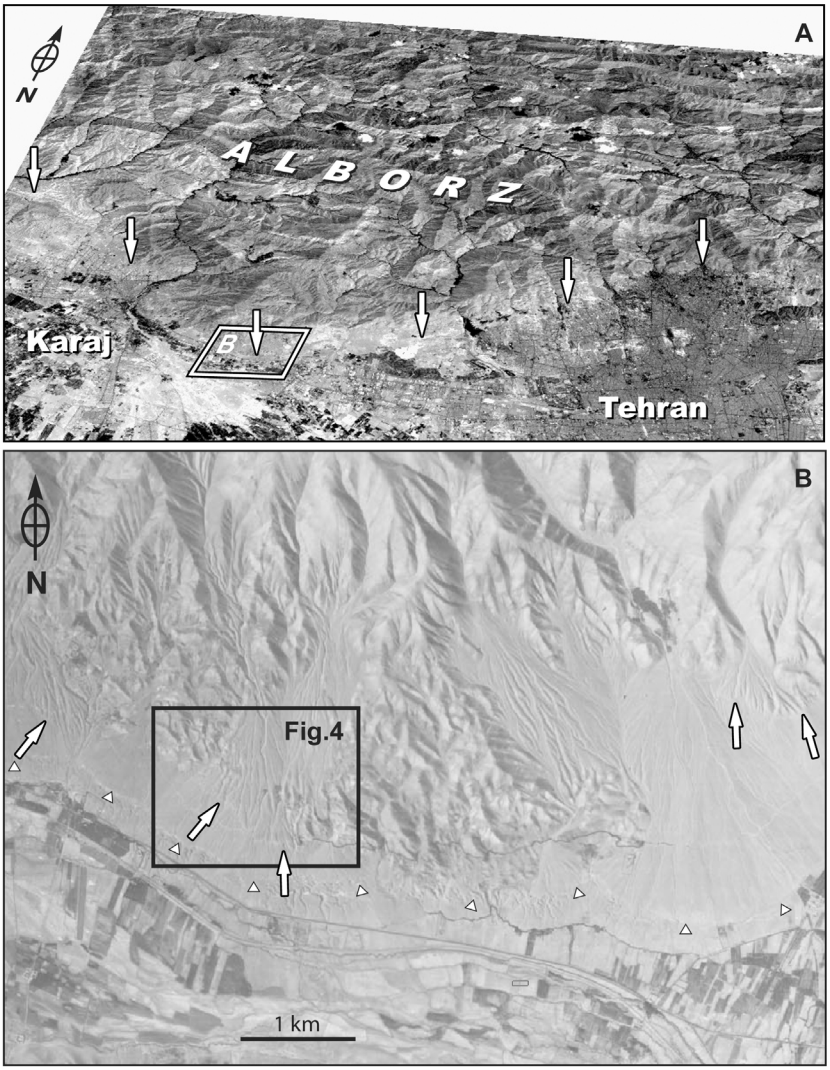

Figure 2. (a) Landsat image in perspective view toward the North showing the megacity of Tehran and the city of Karaj extending over the piedmont of the Alborz Mountains. The white arrows indicate the mountain front where stands the North Tehran Fault (NTF). (b) Aerial photo of the front of the Central Alborz Mountain range between Tehran and Karaj cities, showing the change of strike direction of the NTF (Flight AMS 158, August 1955, 1:50,000 scale). White arrows point out NTF fault scarp affecting alluvial fans. Note also the ancient shorelines (white triangles) below the NTF, suggesting that an immense lake ($\sim$70.000 km^2) was covering the Kavir-e Namak region (Great Salt Desert) region, probably at the beginning of the Holocene [*Nazari et al.*, 2010].

observed along these two first segments [*Solaymani et al.*, 2011]. A third segment, 20 km long, begins with a 10 km long section oriented NE-SW, which redirects E-W along a 10 km long reverse fault section. The tracks of quaternary fault activity steps then to the NW-SE branch of the NTF. This one starts with a clear $\sim$10 km long fault section along which evidences of reverse faulting can be observed (see Figure 2b). The tracks of activity are then difficult to follow in the morphology due to the human activity that strongly modified the morphology of the mountain front. The NTF is supposed to join the NW-SE trending Abyek-Qazvin fault (see Figure 1a), the motion across which is thought to be mainly reverse slip [*Berberian et al.*, 1993].

[7] To the south of the NTF, the alluvial sediments are affected by secondary structures at several sites (e.g., Mahmoudieh fault, Milad tower foreberg) (Figure 3a). Most of these structures can be interpreted as folds controlled by thrusts faults, and correspond to foreberg structures [e.g., *Bayasgalan et al.*, 1999; *Ritz et al.*, 2003; *Walker et al.*, 2003]. Those forebergs appear to be controlled by north-dipping faults, but some south-dipping secondary thrusts may also occur (i.e., Mahmoudieh fault). Considering the short wavelength (<5 km) of these fold-and-thrust structures and the fact that some of them are controlled by south-dipping faults, we suggest that a décollement is controlling the deformations observed within the Tehran alluvial plain (Figure 3b). The overall pattern associating the NTF (*sensus stricto*) and the secondary fold-and-thrust structures can be defined as a surficial partitioned system.

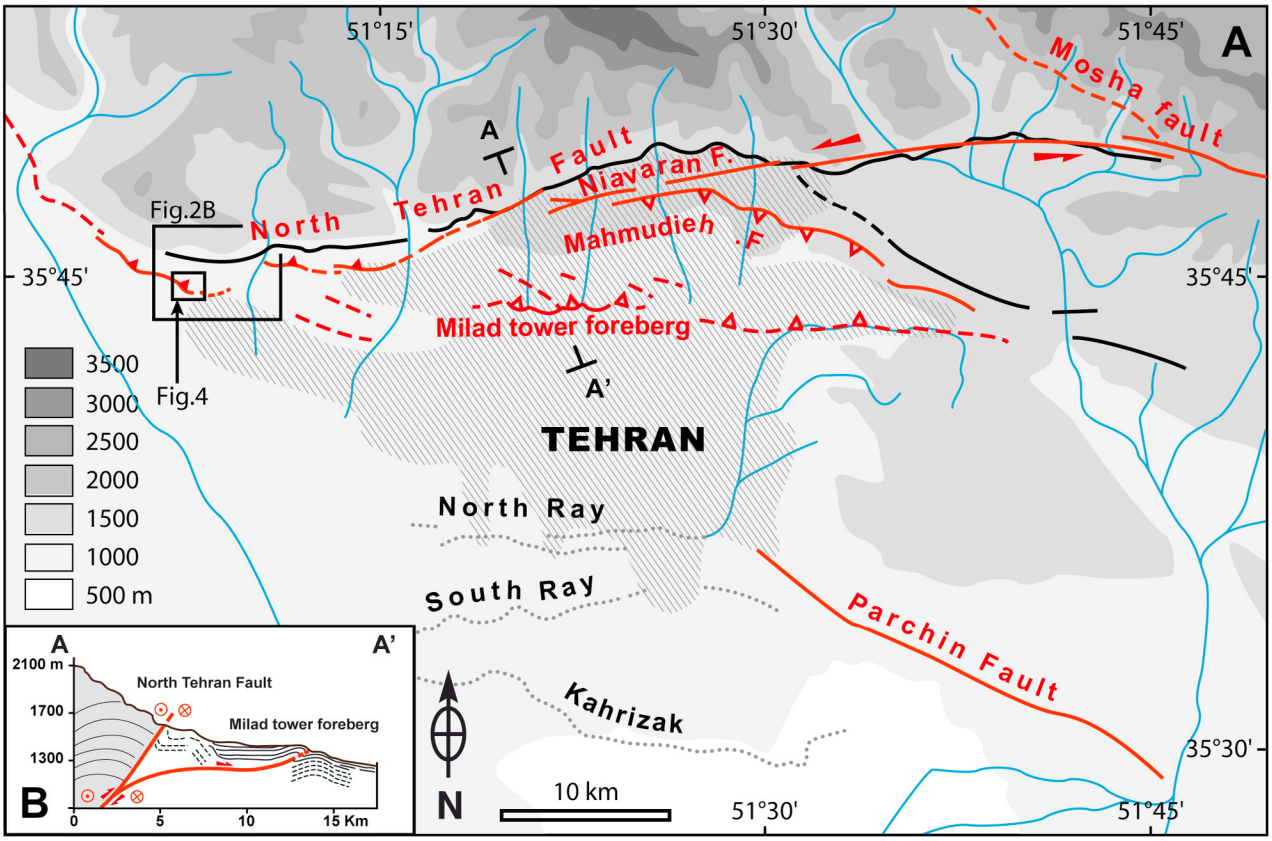

Figure 3. (a) Map of the active faults in Tehran region compiling works by *Berberian et al.* [1993], *Abbassi and Farbod* [2009], *Nazari* [2006], *Landgraf et al.* [2009], *Nazari et al.* [2010], *Solaymani et al.* [2011] and this study: The hatched area defined Tehran city and suburbs (Google Earth imagery (c) Google Inc. Used with permission.). The black lines correspond to inactive Cenozoic faults; the red lines correspond to active faults; the dashed red lines correspond to uncertain traces of active faulting or of hidden faults; the dotted gray lines correspond to ancient shorelines; the blues lines are seasonal streams and rivers; the black square shows the studied area. (b) Simplified geological cross-section across the NTF zone showing the connection between the main deep-seated fault and the secondary Milad tower foreberg; Eocene formations are in gray and Quaternary deposits are in white.

[8] Downstream of the alluvial piedmont, other topographic scarps are observed (i.e., Kahryzak, North and South Ray, Figure 3) that were interpreted initially as fault scarps [*Berberian et al.*, 1985; *De Martini et al.*, 1998]. A recent morphotectonics study re-interpreted these features as ancient shorelines suggesting that an immense lake was filling the great Kavir desert, probably at the early Holocene period [*Nazari et al.*, 2010].

[9] The catalogs of historical seismicity describe several large earthquakes that destroyed the old city of Ray (corresponding nowadays to the southern suburbs of Tehran) during the past 2500 years (Figure 1). Classically, four main events are reported at the end of the 4th century B.C, in 855 A.D., 856 A.D and 1177 A.D. [*Ambraseys and Melville*, 1982, *Berberian and Yeats*, 1999]. However, there are now good arguments to attribute the 856 A.D. historical earthquake to the Asthaneh fault in Eastern Alborz [*Hollingsworth et al.*, 2010; *Rizza*, 2010] and not to a fault within the Tehran region (see Figure 1a). Among the three other events, the most recent one (1177 A.D. event, estimated magnitude 7.2) is described as the closest to the NTF with a maximum of damages in Ray and Karaj cities [*Ambraseys and Melville*, 1982]. The oldest earthquake (4th century B.C. event) would have been the most destructive, and has devastated the region of Ray. *Ambraseys and Melville* [1982] estimated that the earthquake occurred probably between 312 and 280 B.C. (reign of Seleucus Nicator) and had a magnitude equal or larger than 7.6. They estimated that its epicenter was located ~30 km southeast of Ray. *Berberian and Yeats* [2001] placed this event at the junction between the Parchin and Garmsar fault. The 855 A.D. earthquake destroyed the city of Ray and would have caused also some damages within cities located until 170 km further south. *Ambraseys and Melville* [1982] estimated its magnitude at 7.1 and placed its epicenter within Ray.

[10] In terms of instrumental seismicity, the region situated between Karaj and Tehran displays a very low level of activity (Figure 1). The few M > 4.5 event that were recorded are located within the Mosha and Garmsar faults with focal mechanisms indicating strike-slip faulting. The recent

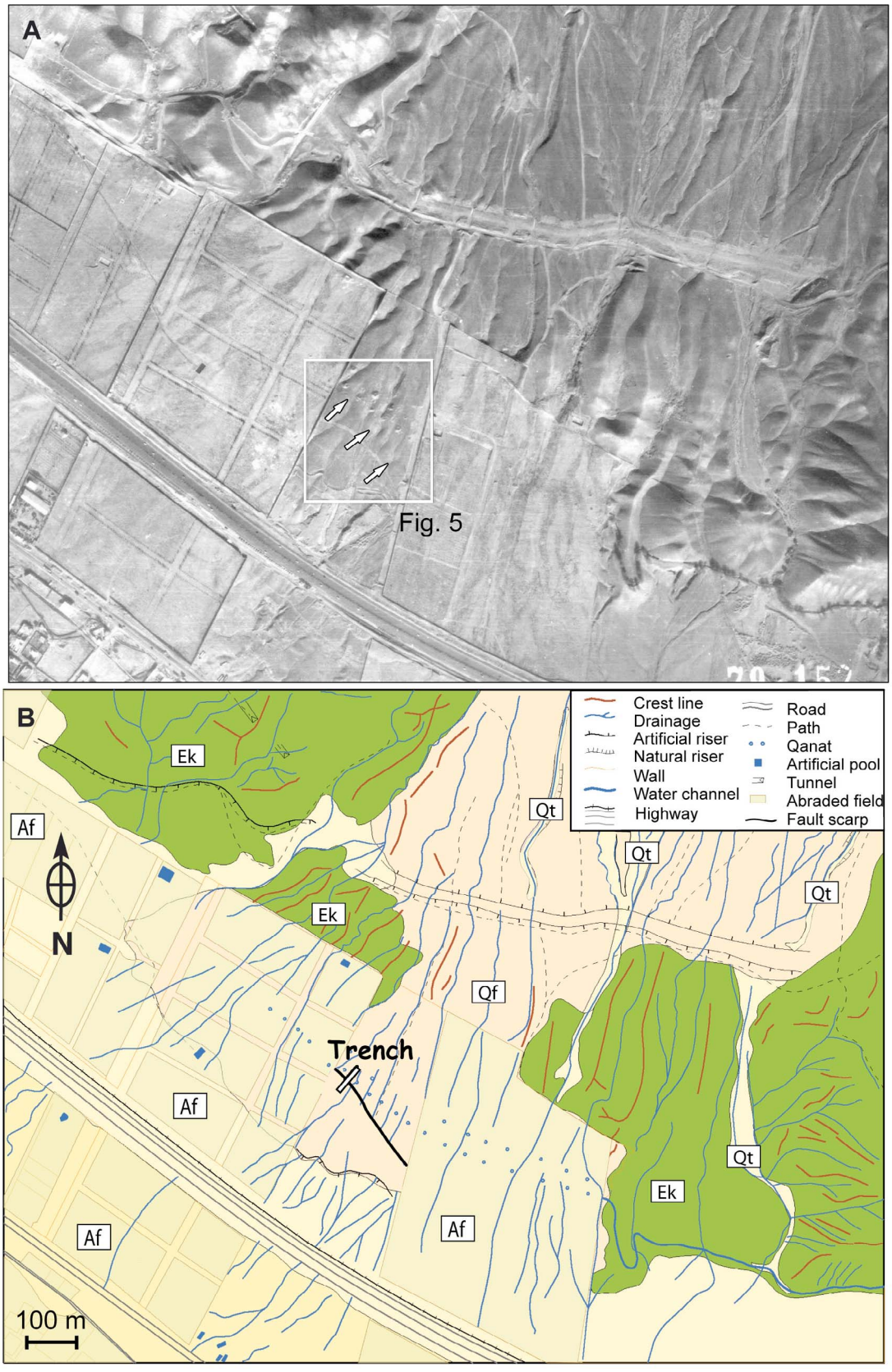
A
Fig. 5
B
Crest line
Drainage
Artificial riser
Natural riser
Wall
Water channel
Highway
Road
Path
Qanat
Artificial pool
Tunnel
Abraded field
Fault scarp
Ek
Af
Qt
Qf
N
Trench
100 m

Figure 4

microseismic study by *Ashtari et al.* [2005] confirms this pattern.

3. Paleoseismological Analysis

[11] From the analysis of 1/50,000 scale aerial pictures (flight AMS 158, August 20, 1955), we identified several fault scarps within the central sector of the NTF, where it switches from a NE-SW to a NW-SE direction between Tehran and Karaj cities (see location in Figures 2 and 3). In the field, we could access only to one of these features, a remnant of a NW-SE trending fault scarp at the termination of the NW-SE branch of the NTF, that we had also recognized on a 1:10000 scale aerial photo taken in 2000 (Figure 4). Today, it is almost impossible to see this fault scarp on Google earth Quickbird 60 cm resolution images (however, the trench site with GSI logo marked on the metallic metal roof protecting the trench is visible; see coordinates in Figure 4 captions). The fault scarp is situated 1.5 km southwards from the base of the main reliefs (see Figure 2b) and bounds an area of lower elevation where blue volcanic tuffs of the Eocene Karaj formation (Ek) form smooth hills in which is inset an alluvial fan surface (Qf) (Figure 4b). The preserved fault scarp is observed within the southern part of the alluvial surface that is made of detrital material from upstream Karaj formation cemented in a sandy matrix, and is mapped as Quaternary deposits after the geological map [*Geological Survey of Iran*, 1993]. The fan surface is incised by numerous stream incisions. One observes few fluvial terraces (Qt) along the mainstreams.

[12] On the aerial picture, the scarp is preserved between two artificial abraded fields and can be followed over a length of ~200 m with a constant direction of N145°E (Figure 4). It is characterized by a clear vertical offset as evidenced by the incision features perpendicular to the scarp that stop abruptly at the scarp line. Today, only the northern half of the scarp can still be seen. The southern half has disappeared due to the construction of the railway joining Karaj to Tehran. Two parallel Qanat lines are observed in the upper side of the scarp with directions almost parallel to the scarp direction (Qanat lines correspond to old underground galleries used to bring water over long distances; they were excavated from vertical wells spaced at intervals of a few tens of meters, making it possible to evacuate the sediment and to ensure a good ventilation of the galleries that have very gentle slopes). Qanats are often observed along surface rupture in Iran, probably because faults are natural drains for water. Here it is likely that the superimposition and the parallelism between the NTF and the Qanats lines is not a fact a chance. It suggests also that the fault is a shallow dipping reverse fault.

[13] We surveyed the best-preserved part of the scarp with a total station, using a 1 m spaced grid of measures for the most detailed parts (break of slopes, Qanats), to produce a digital elevation model (Figure 5). From it, we estimated a total vertical offset of 3.1 ± 0.3 m. We opened a trench, 70 m long, 3 m width and 2–4 m depth, oriented N030°E transverse to the fault scarp (Figures 5, 6a, and 6b). The trench was hand-excavated, between two wells of the southern Qanat line also in order to analyze whether the Qanat gallery was affected by the fault or not. Unfortunately, the trench was not deep enough to cross the gallery.

[14] The section exposed in the trench confirms the colluvial-alluvial nature of the deposits mapped at the area (Figure 6). The stratigraphy is composed of fan-debris material deposited at the foothills of the Alborz mountain range in an arid environment. The units display erosional basal limits with an average slope of 5° and are mainly composed of more or less sorted clastic debris cemented in a sandy matrix (Table 1 and Figure 6). Most of the clasts are volcano-clastic tuff rocks (~85%), mixed with pyroclastic rock fragments, sandstones and chert limestones (15%), all belonging to the Eocene Karaj volcano-sedimentary formation. At the inflection point of the topographic scarp, a clear shallow north-dipping reverse fault (F1) is observed, juxtaposing gray stratified alluvial material over brown deposits (Figure 6). The main fault F1 is trending N115°E and dips 15° to the North, and is associated to a conjugated fault plane (F2) dipping 35°S (Figures 6b and 7). A dozen meters north of the main fault plane F1, we observed two secondary fault planes (F3) and (F4). F3 is trending E-W and dips 13°S, while F4 is trending NS and dips 30–40°E (Figure 7). Near the southern limit of the trench, fifteen meters from the main fault zone, we also observed two other secondary faults (F5 and F6) affecting only deeper stratigraphic units. No obvious correlation was observed between the surface topography and these four secondary faults.

3.1. Interpreting the Trench Log

[15] We logged the eastern wall of the trench with a reference grid of 1 m x 1 m square at a scale of 1:10 (Figure 7). We interpreted between six and seven surface faulting events from fault termination criteria and scarp-derived colluvium (colluvial wedge) features [e.g., *Pantosti et al.*, 1993; *McCalpin*, 1996; *Yeats et al.*, 1997]. We describe and discuss below from the log each event horizon from the most recent to the oldest. Note that because of a limited access to the trench site (the area has been declared closed to the public by the owner) we did not have the time to do a proper photo-mosaic of the eastern wall after its logging. Consequently, we are able to provide here only a photo-montage realized from the first photos taken within the main fault zone during the logging process (Figure 8a). For the same reasons, we could not log the western wall.

[16] **Event 1.** The most recent event is characterized by the presence of the unfaulted unit 11 that is interpreted as a colluvial wedge given its unsorted and unstratified nature and its confinement in front of the main fault F1. Unit 11 is covering the unsorted and unstratified unit 12 (interpreted as

Figure 4. (a) Scan of an aerial photo (1:10,000 scale, from 2000) of the North Tehran fault zone between Tehran and Karaj cities. The white rectangle indicates the studied site (trench site coordinates: latitude 35° 45′ 6.20″ N, longitude 51° 5′ 6.50″ E). The white arrows point out the remnant fault scarp preserved from human activity. (b) Interpretation of the aerial photo. Green, pink, beige and gray colors correspond to Eocene Karaj formation (Ek), the main alluvial fan surface (Qf), the inset terraces (Qt) and areas modified by human activities (Af), respectively.

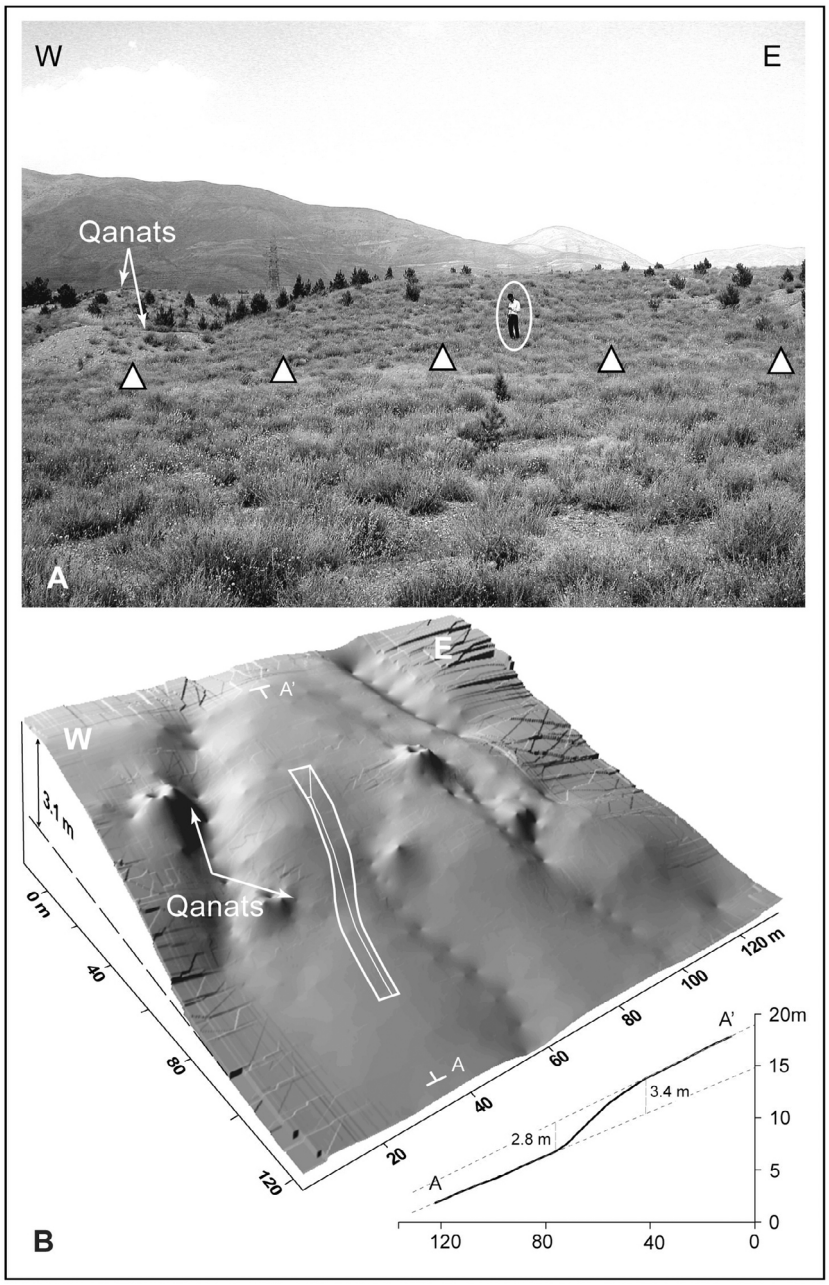

Figure 5. (a) Field view of the fault scarp affecting the quaternary alluvial surface. The tips of white triangles point out the base of the scarp; the circled person gives the scale of the picture. (b) 3D view of the Digital Elevation Model (1 m grid) of the fault scarp with location of the trench and a topographic profile across the scarp showing the total vertical offset of the alluvial surface.

second colluvial wedge) that is cut by the main fault F1. Although no remnant of unit 12 is observed in the hanging wall, the offset of its base (A–A′ = 0.77 m) yields and minimum displacement associated with this most recent surface rupture (event 1).

[17] **Event 2.** The penultimate event is characterized by the colluvial wedge unit 12 that covers unit 21/21A displaced along the fault F1. The base of unit 21/21A shows an offset of 2.35 m (B–B′) along the fault, which yields an offset of 1.58 m for this second event once subtracted the 0.77 m associated with the first event.

[18] **Event 3.** A third event is observed along the fault plane F3 that cut the base of unit 30 with a 0.13 m reverse offset (C–C′) while the overlying unit 10 is not affected. This amount of displacement can be measured at several places along the fault plane suggesting that only one event occurred along fault F3. The question arose whether this feature was contemporary with the event 2 or if it was really a 3rd event, given that the intermediate unit (20/20A) is missing at the fault F3. F1 might have acted as a main trace during the penultimate event E2 and F3 moved affecting the whole stratigraphy up to unit 30 with a minor amount of offset.

Figure 6. Views of the trench. (a) Southwards view (outskirts of Tehran in the background). (b) Northward view showing the eastern wall gridded at 1 m square, the main fault F1 and its conjugated fault F2 (thin dashed red lines underline the faults). (c) View of the shallow-north dipping thrust fault F1 flagged in red on the eastern wall. (d) F1 flagged on the western wall. We estimated the orientation of F1 (N115°E) using the fault location on the opposite trench wall.

[19] However, the occurrence of units 21/21A, confined along F1 - although its basal erosional contact and its fine grained stratigraphy makes it more a fluvial deposits rather than a colluvial wedge - may be interpreted as being associated to some ground deformation along F1 postdating the deposition of unit 20/20A and having controlled the drainage locally. Moreover, along the fault F1, the base of unit 30 shows an offset of 2.39 m (C″–C‴) slightly larger than the offset of 2.35 m (B–B′) measured at the base of units 21/21A suggesting that there was an event between the unit 30 and unit 21/21A. We therefore favor the interpretation that there was a third event before the deposition of units 21/21A.

[20] **Event E4.** This event is observed along the fault F4, which cut through the debris flow unit 50/50A with an upward fault termination sealed by the unit 40. It is difficult to estimate the amount of displacement from the offset of unit 50A, because of the irregular shape of its basal erosive level. Shifts observed on both sides of the fault within underlying units 60, 71 and especially 83D, allow us to estimate a displacement of 0.20 m (D–D′). Along the fault plane, we observed oblique slickensides, with strike, dip and rake of 005, 41 and 155, respectively. These fault slip data indicates right-lateral-reverse faulting along a ~NS trending plane. No evidence was found along F1 for considering that the fault ruptured contemporaneously with F4 during this fourth event.

[21] **Event E5.** The fifth event is observed within the antithetic reverse fault plane F2 that is connected to the principal fault plane F1. Several splays at the tip of F2 affects the lower part of unit 60, but not the above unit 50. The fault displacement associated with this event appears to be rather small. Considering that the warping observed at the base of units 60 and 60A within F2 is due to the deformation associated with the event, and assuming those base levels were linear prior the event, we estimated that the warping was associated with a vertical displacement of 0.10 m (E–E′) along F2. Given the dip of the main fault strand (40°), this yields a displacement of 0.15 m along F2. Note that some folding might have been associated to this fifth event, when considering the upwards convex shape of unit 60 between F2 and F1, its tilting against the fault F1, and the distribution of units 50 and 40 which are confined behind the pop-up structure formed by F1–F2 faults. According to our interpretation, the unit 40 is absent in the footwall compartment. Along the principal rupture F1, the base of unit 60 shows the same 2.39 m displacement (E″–E‴) than the bases of the above units 30 (C″–C‴), which suggests that no additional displacement occurred above the intersection F1/F2 during this fifth event.

[22] This faulting along F2 during this fifth event may be contemporaneous with another rupture (F6) in the southern part of the trench that is sealed by unit 51, although it is difficult to tell precisely when this one occurred given the absence of the intermediate units between unit 51 and 80A. The base of the underlying unit 80A being not displaced, suggests that the rupture corresponds rather to fracture than a fault.

[23] **Event E6.** We interpret another event along the antithetic reverse fault F2 from the difference of offsets observed between units 60/60A and the underlying units 72 and 73. The bases of units 72 and 73 shows a displacement of 0.35 m (F–F′), which represents a bit more than twice the

Table 1. Description of Stratigraphic Units Observed in the Trench T1

Unit	Description
10	Dark brown organic soil.
11	Pink brown silty matrix, 25% clasts (2 mm–3 cm) unsorted and unstratified, colluvial wedge.
12	Brown sandy silty matrix, 50% clasts (5 mm–5 cm) unsorted, unstratified, colluvial wedge.
20	Brown-orange sandy silty matrix, fine grained, 20% angular clasts (2 mm–10 cm), poorly sorted.
20A	Dark brown silty matrix, 50% clasts (2 mm–1 cm), poorly sorted, unstratified.
21	Brown gray silty matrix, fine grained, few big clasts.
21A	Brown gray silty matrix, fine grained.
30	Light brown sandy silty matrix, 50% clasts (5 mm–15 cm), unsorted, unstratified.
40	Brown to gray silty sandy matrix, 70% clasts (1–10 cm), few big clasts (10–20 cm), poorly sorted.
40A	Gray to light brown sandy silty matrix, 70% clasts (5 mm–5 cm), poorly stratified.
40B	Brown to dark gray sandy silty matrix, 65% clasts (5 mm–10 cm), a few big clasts (10–20 cm), poorly sorted (channel?).
50	Brownish cream silty matrix with chalk, 55% clasts (1–10 cm), poorly sorted debris flow.
50A	Cream to brown silty to chalky matrix, 50% clasts (1–15 cm), poorly sorted debris flow.
50B	Brown to gray sandy silty matrix, 70% clasts (1–10 cm), poorly sorted, a few lens with clasts <1 cm.
51	Greyish brown sandy silty matrix, 65% clasts (5 mm–5 cm), roughly sorted and stratified.
51A	Gray to brown sandy silty matrix, 65% clasts (3 mm–4 cm), a few big clasts (4 cm–10 cm), channel.
51B	Brown sandy silty matrix, 20% clasts (5 mm–4 cm), unstratified, (channel?)
51C	Gray sandy silty matrix, 75% clasts (3 mm–7 cm), well sorted, poorly stratified.
51D	Gray-brown sandy silty matrix, 60–70% clasts (2 mm–1 cm), up-ward coarsening (5 cm), well sorted.
51E	Light brown silty matrix, 70% clasts (1–6 cm), sorted, channel.
52	Gray silty sandy matrix, 75% clasts (2 mm–5 mm), well sorted.
53	Brownish gray sandy silty matrix, 65% clasts (5 mm–4 cm), sorted.
54	Gray to brown silty sandy matrix, 60 to 75% clasts (5 mm–4 cm), sorted.
54A	Gray to brown sandy silty matrix, 60% clasts (5 mm–5 cm), sorted.
60A	Gray to brownish gray sandy silty matrix, 85% clasts (4 mm–2 cm), well sorted
60B	Brown silty matrix, 60% clasts (2–6 cm), channel or colluvial wedge?
60	Brown silty matrix, 50% clasts (1–8 cm), numerous large clasts (8–12 cm) unsorted.
61	Brown-gray sandy silty matrix, 50% clasts (3 mm–6 cm), few clasts (15 cm), poorly sorted, lens shape.
61A	Brown sandy silty matrix, 60% clasts (2 mm–7 cm), poorly sorted, channel.
61B	Light brown muddy matrix, 50% clasts (5 mm–8 cm), poorly sorted.
61C	Brown silty matrix, 50% clasts (2 mm–15 cm), poorly sorted, unstratified.
61D	Gray sandy silty matrix, 75% clasts (2 mm–1 cm), well sorted, lens shape
61E	Gray to light brown silty matrix, 70% clasts (5 mm–4 cm), a few big clasts (10 cm–15 cm), well sorted.
62	Gray sandy silty to sandy matrix, 80% clasts (2 mm–7 cm), stratified, well sorted.
62A	Gray sandy silty matrix, 75% clasts (2 mm–4 cm), well sorted.
62B	Brownish gray sandy silty, 70% clasts (5 mm–4 cm), channel.
62C	Brown to gray sandy silty matrix, 65% clasts (3–7 mm), well sorted, lens shape
70	Gray to brownish gray silty sandy matrix, 75% clasts (5 mm–10 cm), stratified.
70A	Gray silty sandy matrix, 70% clasts (3 mm–1.5 cm), sorted, channel.
70B	Gray to brown silty sandy matrix, 70% clasts (2 mm–4 cm), sorted, channel.
71	Gray sandy silty matrix, 80% clasts (5–15 mm), well sorted and stratified.
72	Gray to brownish gray sandy silty matrix, 80% clasts (3 mm–4 cm), stratified
73	Gray to brown silty to sandy silty matrix, 55% clasts (5 mm–5 cm)
80	Gray-brownish gray sandy silty matrix, 75% clasts (5 mm–20 cm), poorly sorted.
80A	Brown sandy silty matrix, 80% clasts (2 mm–2 cm)
81	Gray sandy silty matrix, 70% clasts (3 mm–7 cm), poorly sorted, poorly stratified.
82	Gray sandy silty matrix, 75% clasts (5 mm–3 cm), sorted.
83	Brown silty matrix, 60% clasts (2–4 cm) with big clasts (4–10 cm), poorly sorted.
83A	Brownish gray silty matrix, 75% clasts (5 mm–2 cm), well sorted.
83B	Brown to gray sandy silty matrix, 60% clasts (1–6 cm), upward fining (2 mm), well sorted, channel.
83C	Gray brown matrix with angular debris, unsorted, unstratified.
83D	Cream to brown consolidated, unstratified, colluvial wedge.
84	Brownish gray sandy silty matrix, 50% clasts (2 mm–7 cm), poorly sorted.
84C	Brown silty matrix, 50% clasts (1–7 cm), sorted (channel?)
85	Brown sandy silty matrix, 55% clasts (1–7 cm), poorly sorted
85A	Light brown sandy silt, clasts in upper part (5 mm–4 cm), unstratified.
85B	Greyish brown sandy silty matrix, 65% clasts (5 mm–5 cm), roughly sorted.
85C	Light brown silty matrix, 70% clasts (2–5 cm), well sorted (channel?)
86	Brownish gray silty matrix, 70% clasts (5 mm–5 cm), poorly stratified.
90	Light brown silt, a few clasts (1–2%), unstratified.
91	Brownish gray silty sandy matrix, 50% clasts (2 mm–3 cm), sorted.
92	Brown to gray sandy silty matrix, 25% clasts (2 mm–1 cm), sorted.
93	Gray to brown silty sandy matrix, 65% clasts (4 mm–4 cm), sorted, unstratified.
100	Massive clastic unit, grey silty matrix, 60% clasts (1–20 cm), few big clasts (20–30 cm), roughly stratified.
101	Grey to brown sandy silty matrix, 40% clasts (2 mm–5 cm), poorly sorted, stratified.
101A	Brownish cream silty matrix, 60% clasts (1–7 cm), few cobbles (15–30 cm), poorly sorted, channel.
102	Grey muddy matrix (to sandy matrix southwards), 80% clasts (5 mm–4 cm), stratified.
103	Brown silty matrix, 70% clasts (1–15 cm), few big clasts (>15 cm), poorly sorted.

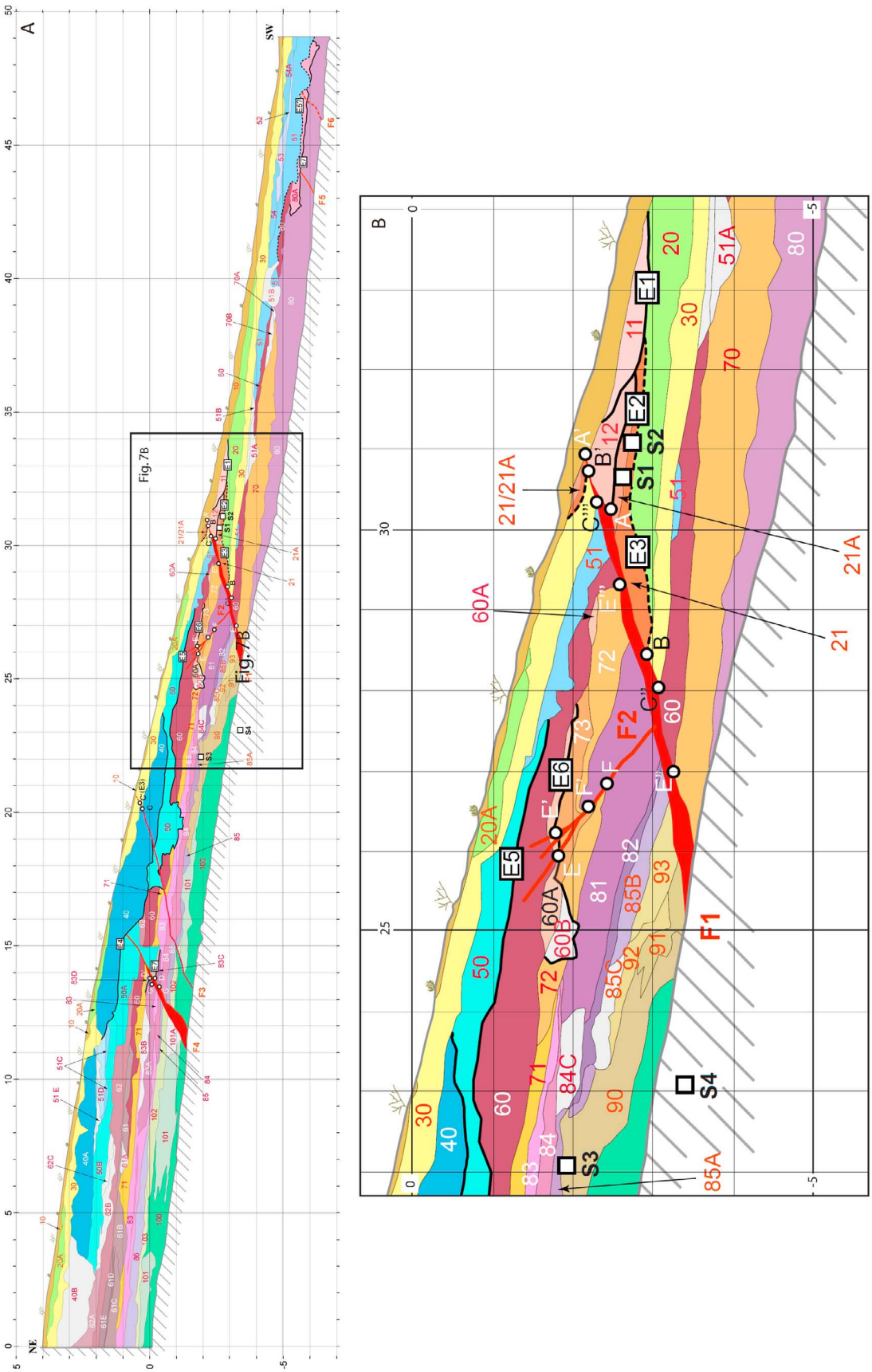

Figure 7. (a) Log of the eastern wall of the trench. Stratigraphic units are represented in different colors and numbers (see Table 1 for description of units). Ruptures and sheared zones are in red; thick black lines correspond to event horizons numbered from 1 to 7 in white rectangles (youngest to the oldest); white circles are piercing points across faults used for displacement evaluation along the fault; white squares are the collected IRSL samples. (b) Zoomed frame of the main fault zone.

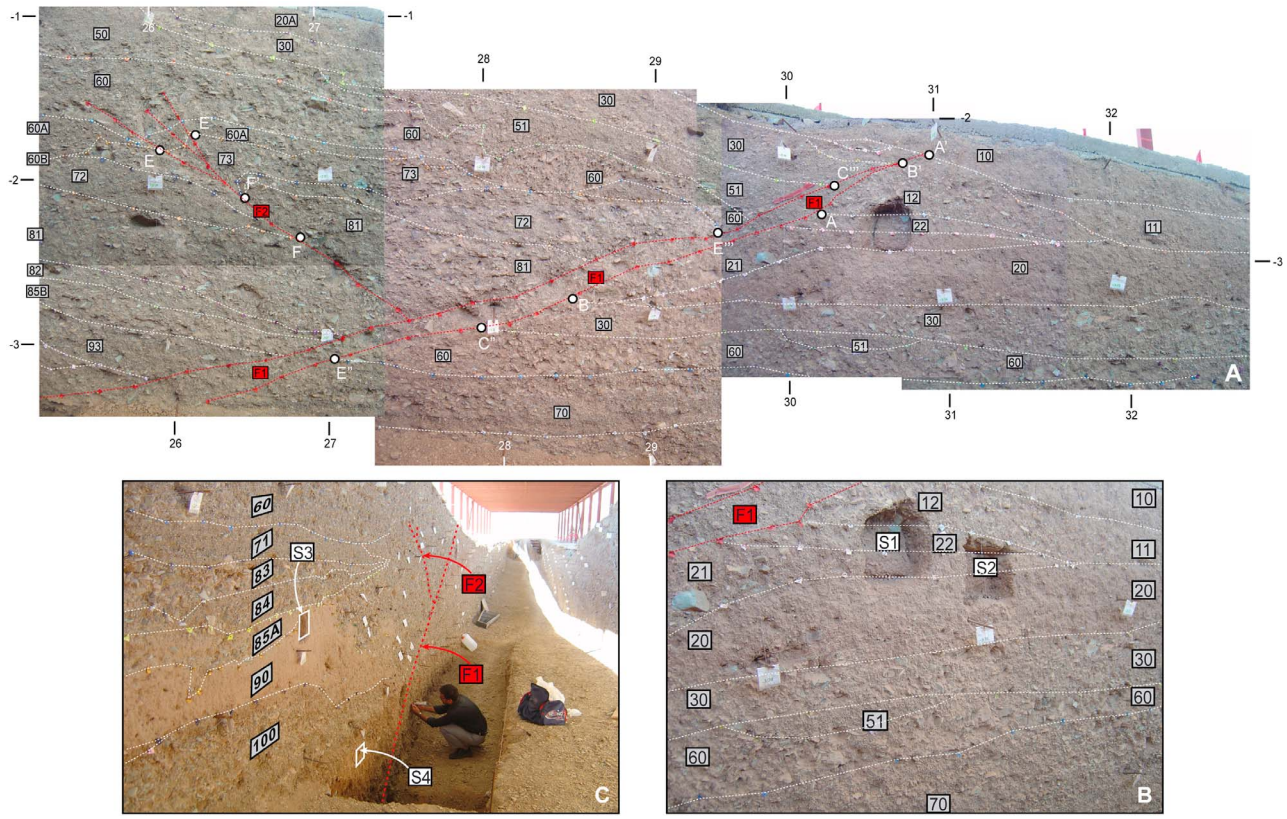

Figure 8. (a) Photo-montage of the main faulted zone. Numbers in gray and red rectangles correspond to stratigraphic units and ruptures, respectively. The unit limits are underlined with thin dashed white lines and the fault/fault zone with thin dashed red lines. White circles and letters indicate piercing points. The area excavated under the colluvial unit 12 corresponds to S1 IRSL sample. (b) Samples S1 and S2 (numbers in white rectangles) collected within units 21A and 21, respectively, below the colluvial wedge unit 12. (c) Samples S3 and S4 collected in unit 90 and below unit 100, respectively.

amount estimated for units 60/60A (0.15 m = E–E′). Consequently, we placed a sixth event horizon below the units 60/60A/60B, for which the estimated offset is 0.20 m (=0.35 m–0.15 m). The occurrence of the channel unit 60B at the front of the deformed units 72 and 73, suggests also that some scarp was formed and controlled the drainage locally.

[24] **Event E7.** A seventh event is observed within the fault plane F4, below the colluvial wedge unit 83D. The bottom of unit 83C indicates an apparent displacement of 0.4 m (G–G′) along the fault that is also observed within the underlying units (this is an apparent displacement since oblique slickensides are observed along the fault; see Event 4 description). This displacement includes the displacement associated with event E4 (D–D′ = 0.2 m), which yields therefore a 0.2 m displacement for the event E7. We cannot tell whether this event is also associated with a displacement along the fault F1; in fact at F1 location, the trench is not deep enough to see the offset within units 80/81, and tell whether it is larger than the offset observed within the upper units. On the other hand, the fault termination feature observed within fault F5, in front of the main fault F1, sealed by unit 80A, may correspond to the event E7. Unfortunately, no clear offset features within unit 80 allowed to estimate an offset. Below unit 83D, the underlying unit 83C (unstratified colluvial unit of limited extent) was not interpreted as another colluvial wedge, given that we observe a constant 0.4 m offset (equal to G–G′) within the underlying units.

[25] In summary, we interpreted between 6 and 7 events from the logging of the eastern wall of the trench that are characterized by fault terminations and colluvial wedges features, and are distributed on one main rupture (F1) and its antithetic conjugated fault (F2), and four secondary faults (F3, F4, F5 and F6). Four or five events (E1, E2, E3?, E5, and E6) occurred along the F1–F2 main fault zone. Event E3 (or E2?) also ruptured a reverse fault (F3) similar in terms of kinematics (shallow dipping thrust fault) than fault F1, and event 5 may also have ruptured a secondary reverse frontal fault (F6). Two events, E4 and E7, are located on the secondary oblique-slip fault F4, the last one (E7) having probably also ruptured another secondary reverse fault (F5).

3.2. Estimating the Magnitudes of Paleoearthquakes

[26] From the displacements associated with the different events observed in the trench (i.e., from the most recent to the oldest: 0.77 m, 1.58 m, 0.13 + 0.04 m, 0.20 m, 0.15, 0.20, and 0.20 m, respectively if considering 7 events; 0.77 m, 1.58 + 0.13 + 0.04 m, 0.20 m, 0.15, 0.20, and 0.20 m, respectively if considering 6 events), we estimated Moment Magnitude Mw of earthquakes, using empirical functions of *Wells and Coppersmith* [1994]. These estimates

Table 2. Luminescence Results: Unit Number, Sample Number, Paleodose, Annual Dose Rate and IRSL Age Estimates[a]

Unit	Sample	Paleodose $De \pm \sigma$ (Gy)	Total Dose Rate Da (Gy/ka)	Apparent IRSL Age ($\pm\sigma$ (ka))	Corrected IRSL Age[b] ($\pm\sigma$ (ka))
21A	S1	26.1 ± 3.5	3.86 ± 0.30	6.7 ± 1.0	7.9 ± 1.2
21	S2	26.3 ± 2.8	3.58 ± 0.28	7.3 ± 0.9	8.6 ± 1.1
90	S3	74.7 ± 5.2	3.33 ± 0.27	22.4 ± 2.4	26.7 ± 2.9
U	S4	85.5 ± 7.5	3.52 ± 0.28	24.3 ± 2.8	29.0± 3.6

[a]The four samples were prepared in the Laboratoire de Préhistoire et Quaternaire in University of Lille 1, and were analyzed in the Department of Earth Sciences in University of Québec in Montréal. U for unlogged.
[b]IRSL ages corrected for anomalous fading using the protocol of *Huntley and Lamothe* [2001].

could be regarded as minimum values given that they do not take into account a potential oblique component as suggested by the slickensides observed along one of the fault plane (i.e., F4). However, the differences of shape and thickness of stratigraphic units observed on both sides of the main fault F1 do not allow to estimate whether this potential additional horizontal component increases or in the contrary decrease the amount of displacement per event. Moreover, the NNE-SSW direction of the slip vector along F4 is perpendicular to the main ESE-WNW trending fault plane F1, suggesting that F1 kinematics is probably close to pure reverse faulting.

[27] We used the function Mw = a + b * log (AD), where a = 6.64 ± 0.16 and b = 0.13 ± 0.36, yielding Mw from an average displacement (AD) in the case of a reverse fault. Whatever the scenario (7 or 6 events), calculated magnitudes are comprised between 6.3 and 6.9. Similarly, if considering the displacements observed in the trench as maxima, also in the case of a reverse fault (MD replacing AD in *Wells and Coppersmith*'s [1994] equation), with coefficients a = 6.52 ± 0.11 and b = 0.44 ± 0.26, calculated magnitudes are comprised between 6.1 and 6.8. When using the function defined for all fault cases (i.e., reverse, normal and strike-slip faults gathered together) with a = 6.93 ± 0.05 and b = 0.82 ± 0.10, estimated Mw magnitudes range between 6.2 and 7.2, also whatever the scenario (7 or 6 events). The higher values among the different estimates (6.9, 6.8 and 7.2) are consistent with the magnitude of an earthquake that would break the entire 110 km long NFT. However, the lower estimates (6.3, 6.1 and 6.2) suggest also that smaller events can occur along the NTF, breaking only a part of the fault, which is consistent with the present-day segmentation of the NTF (see Figure 3).

3.3. Dating the Paleoearthquakes

[28] To constrain the age of the paleoevents observed in the trench, we used optically stimulated luminescence (OSL), a method successfully applied in this kind of arid and dry environment [e.g., *Prentice et al.*, 2002; *Walker et al.*, 2006; *Balescu et al.*, 2007; *Le Dortz et al.*, 2009; *Rizza et al.*, 2011], where given the lack of organic material, this can be the only helpful method [e.g., *Fattahi*, 2009; *Nazari et al.*, 2009b, *Foroutan et al.*, 2012]. Here, we apply the Infrared Stimulated Luminescence (IRSL) dating method to the feldspar detrital fine grains (4–11 μm). When feldspars are optically stimulated by near infrared photons they produce an IRSL signal which is used as geochronometer for dating the last exposure of the sediment grains to sunlight or the time elapsed since their deposition. Despite the general coarse granulometry of the deposits, we managed to collect four samples within the finest stratigraphical units.

[29] Samples were collected as blocks in order to preserve their structure (Figures 8b and 8c). Samples S1 and S2 were collected in the footwall, in units 21A and 21, respectively, immediately below the two colluvial wedges units 11 and 12 (Figures 7 and 8b). Samples S3 was collected in the hanging wall (Figures 7 and 8c), in unit 90 that is underlain by faulted units 80–83 (see Figure 7). A fourth sample (S4) was collected in a lower part of the trench during a latter excavation (Figures 7 and 8c). Unfortunately, the trench site has been closed as explained above, and we did not have the time to complete the logging of this part. However, we analyzed also this sample to check the consistency of results in terms of stratigraphic order.

[30] The four samples were prepared in the Laboratoire Halma Ipel in University of Lille 1, and were analyzed in the Department of Earth Sciences in University of Québec in Montréal (Table 2). The IRSL signal was recorded using a Corning 7–59/Schott BG39 blue transmitting filter combination (300–500 nm). The paleodoses (De) obtained using the multiple aliquot additive γ dose method were estimated on irradiated samples, preheated at 160°C for 8 h after irradiation. The IRSL induced by the preheating treatment (thermal transfer) was subtracted from the IRSL signal. The external contributions to the total dose rate were estimated from the concentrations of U, Th and K measured by neutron activation analysis. Dose rate values were corrected for water content. The relative alpha efficiency was estimated at 0.09± 0.01. The cosmic dose rates were estimated from the calculation of *Prescott and Hutton* [1994] using the present-day burial depth of the samples. All the samples showing a significant decrease of induced luminescence with time, the apparent IRSL ages have been corrected for anomalous fading using the protocol of age correction suggested by *Huntley and Lamothe* [2001]; the average fading rate (g value) was estimated at 3 ± 0.5% per decade using the method A of *Auclair et al.* [2003].

[31] The IRSL ages (Table 2) are stratigraphically consistent and range between 7.9 ± 1.2 ka (S1) and 29.0 ± 3.6 ka (S4). The 7 or 6 events occurred during the past 26.7 ± 2.9 ka (S3). Five or 4 events occurred between 26.7 ± 2.9 ka (S3) and 8.6 ± 1.1 ka (S2), while the two youngest events E1 and E2 are posterior to 7.9 ± 1.2 ka (S1). If we divide these three periods of time by the number of events they contain, we obtain the following mean recurrence intervals: 3.8 ± 0.4 kyrs, 3.6 ± 0.8 kyrs and 3.9 ± 0.6 kyrs, respectively in the case of 7 events, and 4.4 ± 0.5 kyrs, 4.5 ± 1.0 kyrs and 3.9 ± 0.6 kyrs, respectively in the case of 6 events.

3.4. Estimating the Slip Rate Along the NTF

[32] The nature of the colluvial-alluvial material (very fine grain volcano-clastic tuff rocks) and the stratigraphy (superposition of units generally lower than 50 cm thick) precluding the possibility of dating the offset alluvial surface with in situ produced cosmogenic isotopes as the ^{10}Be or the ^{36}Cl [e.g., *Ritz et al.*, 2003; *Shabanian et al.*, 2009], we estimated the slip rate using the offset features observed in the trench. We used the 2.35 m offset observed along the main rupture F1, that we divided by the OSL age (7.9 ± 1.2 ka) obtained for unit 21A predating the offset. This yields a 0.3 ± 0.05 mm/yr slip rate along the fault for the past ∼8 ka. Given the low angle dip of the fault (15°N), the horizontal shortening rate across the fault is quasi-identical (∼0.3 mm/yr), while the vertical slip rate is lower than 0.1 mm/yr.

4. Conclusions and Discussion

[33] This first paleoseismological study along the North Tehran fault allowed a first quantification of its activity. The studied fault segment, located at the southern termination of the NW-SE branch of the NTF, between the cities of Teheran and Karaj cities, corresponds mainly to a reverse fault (N115°E, 15N) with some dextral component along a NS trending secondary fault. Geometry and kinematics of this segment is consistent with the occurrence of left-lateral active structures described further east along the NE-SW branch of the NTF by *Landgraf et al.* [2009] and *Solaymani et al.* [2011] (see Figure 3). The fault affects Upper-Pleistocene - Holocene alluvial deposits and formed a mean 3 m high cumulative scarp at the studied site. Our trench investigation allowed us to identify between 6 and 7 surface-rupturing events. Their minimum magnitudes (Mw) estimated from the displacements on faults and calculated from the functions of *Wells and Coppersmith* [1994], are between 6.1 and 7.2. The highest of these values is consistent with a 110 km long NTF rupture, but lower estimates suggest also that smaller events are possible, consistently with the present segmentation of the NTF.

[34] The 6 or 7 earthquakes occurred during the last 30 kyrs. If we consider a seven-event scenario (our favored interpretation), the similarity of the mean return periods among the different time sequences could be interpreted as a regular distribution of paleoearthquakes through time with a mean return period of 3.8 ± 0.7 kyrs. However, without further age constraints, an irregular distribution cannot be ruled out.

[35] The two most recent events occurred during the last 7.9 ± 1.2 ka. It is difficult to tell whether they correspond to historical earthquakes that damaged the region of Tehran (see Figure 1). The comparison between our paleoseismological data with the historical records suggests that only 2 of the 3 historical earthquakes having destroyed the region of Ray would be associated to the NTF. The last historical earthquake (1177 A.D.) could correspond to the most recent event recognized in the trench (E1, offset ≥ 0.77 m). This is a reasonable hypothesis given its epicenter area between Karaj and Ray (ancient Tehran) and an estimated magnitude of 7.2. The penultimate event in the trench with its larger offset (E2, between 1.58 m and 1.75 m according to a scenario with 7 or 6 events, respectively) could then correspond to the 312–280 B.C. historical earthquake for which a larger magnitude (7.6) is estimated. In this interpretation, the 855 A.D. earthquake would not be associated to the NTF, at least not to the studied fault segment. This is an acceptable interpretation when considering that damages may have occurred at a distance until 170 km far south from Ray, suggesting that a fault as Pishva, located further south (see Figure 1), might be the source of the 855 A.D. event. Correlating our paleoseismological data with the historical seismicity suggests also that the NTF generates earthquakes episodically and not regularly. The time interval between the 1177 A.D. and the 312–280 B.C. earthquakes is ∼1500 years, twice less than the mean recurrence intervals estimated from the paleoearthquakes recognized in the trench.

[36] We estimated a shortening rate across the NTF fault during the past ∼8 ka of ∼0.3 mm/yr, a minimum value given the presence of other active thrust fault segments associated with the NTF in the area (see Figure 3b). The value is consistent with recent GPS data showing that most of the shortening across the Central Alborz is accommodated along its northern front [*Djamour et al.*, 2010]. Whether one considers a regular or irregular distribution of events through time, the slip rate along this fault segment of the NTF was probably slower between ∼26 ka and ∼8 ka given the smaller offsets associated with prehistoric earthquakes during this period.

[37] The displacement accumulated during the past ∼8 ka produced only a total vertical displacement of 0.6 m, while the total height of the fault scarp is ∼3 m. This suggests that the fault is active since at least the Mid-Pleistocene. An interesting point to note here is that during this period, alluvial units kept on accumulating, building up the fan, although the reverse faulting had started. According to our age constraints, the aggradation has stopped around 8 ka ago, and has been followed by incision of the fan sequence and the fault scarp. This is consistent with recent studies attesting of important climate changes between the Upper Pleistocene and the Holocene, leading to the lowering of the base levels and to the incision of landforms [*Nazari et al.*, 2010; *Walker and Fattahi*, 2011].

[38] Finally, given the distribution of active structures within the Tehran region, it is likely that other faults can produce damaging earthquake (Mw > 6), as for instance the Milad Tower foreberg structure or the Parchin fault (see Figure 3). Further paleoseismological investigations are therefore needed to keep on documenting and quantifying the seismic activity of the different faults of this complex active zone upon which millions people are living.

[39] **Acknowledgments.** This work was supported by a French-Iranian research program on the study of the seismic risk within the Tehran region (coordinator D. Hatzfeld). We are grateful to the Geological Survey of Iran (GSI) especially M.T. Korei, the CNRS, and the French Embassy in Iran especially former Ambassador Mister F. Nicoullaud, for their interest and support for this study. We also thank the members of the GSI: M. Talebian, K. Baharfirouzi, F. Ansari, M. Bolurchi, M. Asad Beigi and A. Karbalai Hasan for the help during trenching investigations. We thank D. Pantosti and an anonymous reviewer who made extensive reviews of a first version of the manuscript, as well as R. Walker and F. Cinty whose second reviews helped to finalize the improvement of the manuscript. We thank F. Radjai, M. Ferry and M. Rizza for fruitful discussions, as well as A. Delplanque for her help with drawings.

References

Abbassi, M. R., and Y. Farbod (2009), Faulting and folding in Quaternary deposits of Tehran's piedmont (Iran), *J. Asian Earth Sci.*, *34*, 522–531, doi:10.1016/j.jseaes.2008.08.001.

Allen, M. B., M. R. Ghassemi, M. Shahrabi, and M. Qorashi (2003), Accommodation of late Cenozoic oblique shortening in the Alborz range, northern Iran, *J. Struct. Geol.*, *25*, 659–672, doi:10.1016/S0191-8141(02)00064-0.

Ambraseys, N. N., and C. P. Melville (1982), *A History of Persian Earthquakes*, Cambridge Univ. Press, New York.

Ashtari, M., D. Hatzfeld, and N. Kamalian (2005), Microseismicity in the region of Tehran, *Tectonophysics*, *395*, 193–208, doi:10.1016/j.tecto.2004.09.011.

Auclair, M., M. Lamothe, and S. Huot (2003), Measurement of anomalous fading for feldspar IRSL using SAR, *Radiat. Meas.*, *37*, 487–492, doi:10.1016/S1350-4487(03)00018-0.

Balescu, S., J.-F. Ritz, M. Lamothe, and M. Todbileg (2007), Luminescence dating of a gigantic paleolandslide in the Gobi-Altay Mountains, Mongolia, *Quat. Geochronol.*, *2*, 290–295, doi:10.1016/j.quageo.2006.05.026.

Ballato, P., N. R. Nowaczyk, A. Landgraf, M. R. Strecker, A. Friedrich, and S. H. Tabatabaei (2008), Tectonic control on sedimentary facies pattern and sediment accumulation rates in the Miocene foreland basin of the southern Alborz Mountains, northern Iran, *Tectonics*, *27*, TC6001, doi:10.1029/2008TC002278.

Bayasgalan, A., J. Jackson, J.-F. Ritz, and S. Carretier (1999), 'Forebergs,' flowers structures, and the development of large intra-continetal strike-slip fault: The Gurvan Bogd fault system in Mongolia, *J. Struct. Geol.*, *21*, 1285–1302, doi:10.1016/S0191-8141(99)00064-4.

Berberian, M., and R. S. Yeats (1999), Patterns of historical earthquake rupture in the Iranian Plateau, *Bull. Seismol. Soc. Am.*, *89*(1), 120–139.

Berberian, M., and R. S. Yeats (2001), Contribution of archaeological data to studies of earthquake history in the Iranian Plateau, *J. Struct. Geol.*, *23*, 563–584, doi:10.1016/S0191-8141(00)00115-2.

Berberian, M., M. Ghorashi, B. Arjangravesh, and A. Mohajer Ashjaie (1985), *Seismotectonic and Earthquake Fault Hazard Investigations in the Tehran Region* [in Persian], Geol. Surv. of Iran, Tehran.

Berberian, M., M. Ghorashi, B. Arjangravesh, and A. Mohajer Ashjaie (1993), *Seismotectonic and Earthquake-Fault Hazard Investigations in the Great Ghazvin Region* [in Persian], 61 pp., Geol. Surv. of Iran, Tehran.

De Martini, P. M., K. Hessami, D. Pantosti, G. D. Addezio, H. Alinaghi, and M. Ghafory-Ashtiani (1998), A geological contribution to the evaluation of the seismic potential of the Kahrizak fault (Tehran, Iran), *Tectonophysics*, *287*, 187–199, doi:10.1016/S0040-1951(98)80068-1.

Djamour, Y., P. Vernant, R. Bayer, Y. Hatam, J.-F. Ritz, J. Hinderer, B. Luck, H. Nankali, N. Le Moigne, and M. Sedighi (2010), Geodetic signatures of present-day tectonic deformation in central Alborz and Tehran region (Iran), *Geophys. J. Int.*, *183*, 1287–1301, doi:10.1111/j.1365-246X.2010.04811.x.

Engdahl, E. R., R. Van der Hilst, and R. Buland (1998), Global teleseismic earthquake relocation with improved travel times and procedures for depth determination, *Bull. Seismol. Soc. Am.*, *88*, 722–743.

Fattahi, M. (2009), Dating past earthquakes and related sediments by thermoluminescence methods: A review, *Quat. Int.*, *199*, 104–146, doi:10.1016/j.quaint.2008.06.015.

Foroutan, M., M. Sébrier, H. Nazari, B. Meyer, M. Fattahi, A. Rashidi, K. Le Dortz, and M. D. Bateman (2012), New evidence for large earthquakes on the Central Iran plateau: Palaeoseismology of the Anar fault, *Geophys. J. Int.*, *189*, 6–18, doi:10.1111/j.1365-246X.2012.05365.x.

Geological Survey of Iran (1993), Geology map of Tehran, scale 1:1,000,000, Tehran.

Guest, B., G. J. Axen, P. S. Lam, and J. Hassanzadeh (2006), Late Cenozoic shortening in the west-central Alborz Mountains, northern Iran, by combined conjugate strike-slip and thin-skinned deformation, *Geosphere*, *2*, 35–52, doi:10.1130/GES00019.1.

Hollingsworth, J., J. Jackson, R. Walker, and H. Nazari (2008), Extrusion tectonics and subduction in the eastern south Caspian region since 10 Ma, *Geology*, *36*, 763–766, doi:10.1130/G25008A.1.

Hollingsworth, J., H. Nazari, J.-F. Ritz, R. Salamati, M. Talebian, A. Bahroudi, R. T. Walker, M. Rizza, and J. Jackson (2010), Active tectonics of the east Alborz mountains, NE Iran: Rupture of the left-lateral Astaneh fault system during the great 856 A.D. Qumis earthquake, *J. Geophys. Res.*, *115*, B12313, doi:10.1029/2009JB007185.

Huntley, D. J., and M. Lamothe (2001), Ubiquity of anomalous fading in K-feldspars and the measurement and correction for it in optical dating, *Can. J. Earth Sci.*, *38*, 1093–1106, doi:10.1139/e01-013.

Jackson, J., K. Priestley, M. Allen, and M. Berberian (2002), Active tectonics of the South Caspian Basin, *Geophys. J. Int.*, *148*, 214–245.

Landgraf, A., P. Ballato, M. R. Strecker, A. Friedrich, S. H. Tabatabaei, and M. Shahpasandzadeh (2009), Fault kinematic and geomorphic observations along the North Tehran Thrust and Mosha Fasham Fault, Alborz mountains Iran: Implications for fault system evolution and interaction in a changing tectonic regime, *Geophys. J. Int.*, *177*, 676–690, doi:10.1111/j.1365-246X.2009.04089.x.

Le Dortz, K., et al. (2009), Holocene right-slip rate determined by cosmogenic and OSL dating on the Anar fault, Central Iran, *Geophys. J. Int.*, *179*, 700–710, doi:10.1111/j.1365-246X.2009.04309.x.

McCalpin, J. P. (1996), *Paleoseismology*, 588 pp., Academic, San Diego, Calif.

Nazari, H. (2006), Analyse de la tectonique récente et active dans l'Alborz Central et la région de Téhéran: Approche morphotectonique et paléoseismologique, PhD thesis, Univ. of Montpellier 2, Montpellier, France.

Nazari, H., J.-F. Ritz, A. Shafei, A. Ghassemi, R. Salamati, J.-L. Michelot, and M. Massault (2009a), Morphological and paleoseismological analyses of the Taleghan fault, Alborz, Iran, *Geophys. J. Int.*, *178*, 1028–1041, doi:10.1111/j.1365-246X.2009.04173.x.

Nazari, H., M. Fattahi, B. Meyer, M. Sebrier, M. Talebian, M. Foroutan, K. Le Dortz, M. D. Bateman, and M. Ghorashi (2009b), First evidence for large earthquakes on the Deshir Fault, Central Iran Plateau, *Terra Nova*, *21*, 417–426, doi:10.1111/j.1365-3121.2009.00892.x.

Nazari, H., J.-F. Ritz, R. Salamati, A. Shahidi, H. Habibi, M. Ghorashi, and A. Karimi Bavandpur (2010), Distinguishing between fault scarps and shorelines: The question of the nature of the Kahrizak, North Ray and South Ray features in the Tehran plain (Iran), *Terra Nova*, *22*, 155–237, doi:10.1111/j.1365-3121.2010.00938.x.

Pantosti, D., D. P. Schwartz, and G. Valensise (1993), Paleoseismology Along the 1980 Surface Rupture of the Irpinia Fault: Implications for Earthquake Recurrence in the Southern Apennines, Italy, *J. Geophys. Res.*, *98*(B4), 6561–6577, doi:10.1029/92JB02277.

Prentice, C. S., K. Kendrick, K. Berryman, A. Bayasgalan, J. F. Ritz, and J. Q. Spencer (2002), Prehistoric ruptures of the Gurvan Bulag fault, Gobi Altay, Mongolia, *J. Geophys. Res.*, *107*(B12), 2321, doi:10.1029/2001JB000803.

Prescott, J. R., and J. T. Hutton (1994), Cosmic ray contributions to dose rates for luminescence and ESR dating: Large depths and long-term time variations, *Radiat. Meas.*, *23*, 497–500, doi:10.1016/1350-4487(94)90086-8.

Ritz, J.-F. (2009), Extrusion tectonics and subduction in the eastern South Caspian region since 10 Ma: COMMENT, *Geology*, *37*, E191–E191, doi:10.1130/G25627C.1.

Ritz, J.-F., et al. (2003), Late Pleistocene to Holocene slip rates for the Gurvan Bulag thrust fault (Gobi-Altay, Mongolia) estimated with 10Be dates, *J. Geophys. Res.*, *108*(B3), 2162, doi:10.1029/2001JB000553.

Ritz, J.-F., H. Nazari, A. Ghassemi, R. Salamati, A. Shafei, S. Solaymani, and P. Vernant (2006), Active transtension inside Central Alborz: A new insight of the Northern Iran-Southern Caspian geodynamics, *Geology*, *34*, 477–480, doi:10.1130/G22319.1.

Rizza, M. (2010), Vitesses et déplacements co-sismiques sur des failles décrochantes en Mongolie et en Iran. Apport de la morphotectonique et de la paléosismologie, PhD thesis, Univ. of Montpellier 2, Montpellier, France.

Rizza, M., S. Mahan, J.-F. Ritz, H. Nazari, J. Hollinsgworth, and R. Salamati (2011), Using luminescence dating from coarse matrix material to estimate fault slip-rate in arid domain: Example of the Astaneh Fault (Iran), *Quat. Geochronol.*, *6*, 390–406, doi:10.1016/j.quageo.2011.03.001.

Shabanian, E., L. Siame, O. Bellier, L. Benedetti, and M. R. Abbassi (2009), Quaternary slip rates along the north-eastern boundary of the Arabia-Eurasia collision zone (Kopeh Dagh Mountains, Northeast Iran), *Geophys. J. Int.*, *178*, 1055–1077, doi:10.1111/j.1365-246X.2009.04183.x.

Solaymani, S., J.-F. Ritz, and M. Abbassi (2011), Analysing the junction between the Mosha and the North Tehran active faults, *Tectonophysics*, *497*, 1–14.

Tchalenko, J. S. (1975), Seismotectonics framework of the North Tehran fault, *Tectonophysics*, *29*, 411–420, doi:10.1016/0040-1951(75)90169-9.

Tchalenko, J. S., M. Berberian, H. Iranmanesh, B. Baily, and M. Arsovsky (1974), Tectonic framework of the Tehran region, in *Materials for the Study of Seismotectonics of Iran*, pp. 7–46, Geol. Surv. of Iran, Tehran.

Vernant, P., F. Nilforoushan, J. Chéry, R. Bayer, Y. Djamour, F. Masson, H. Nankali, J.-F. Ritz, M. Sedighi, and F. Tavakoli (2004), Deciphering oblique shortening of Central Alborz in Iran using geodetic data, *Earth Planet. Sci. Lett.*, *223*, 177–185, doi:10.1016/j.epsl.2004.04.017.

Walker, R. T., and M. Fattahi (2011), A framework of Holocene and Late Pleistocene environmental change in eastern Iran inferred from the dating of periods of alluvial fan abandonment, river terracing, and lake deposition, *Quat. Sci. Rev.*, *30*, 1256–1271, doi:10.1016/j.quascirev.2011.03.004.

Walker, R. T., J. Jackson, and C. Baker (2003), Surface expression of thrust faulting in eastern Iran: Source parameters and surface deformation of the 1978 Tabas and 1968 Ferdows earthquake sequences, *Geophys. J. Int.*, *152*, 749–765, doi:10.1046/j.1365-246X.2003.01886.x.

Walker, R. T., et al. (2006), Geomorphology and structure of the Jid right-lateral strike-slip fault in the Mongolian Altay mountains, *J. Struct. Geol.*, *28*, 1607–1622, doi:10.1016/j.jsg.2006.04.007.

Wells, D. L., and K. J. Coppersmith (1994), Emprical relationships among magnitude, rupture length, rupture area, and surface displacement, *Bull. Seismol. Soc. Am.*, *84*, 974–1002.

Yeats, R., K. Sieh, and C. Allen (1997), *The Geology of Earthquakes*, 568 pp., Oxford Univ. Press, New York.